Numerical study of the ignition behavior of a post-discharge kernel in a turbulent stratified crossflow

By T. Jaravel, J. Labahn, B. Sforzo†, J. Seitzman‡ AND M. Ihme

1. Motivation and objectives

Modern jet engines are designed to be highly efficient while simultaneously limiting the amount of harmful emissions produced. Presently, there is a desire to deploy new jet fuels which are renewable, sustainable and allow for energy independence. However, the performance of these fuels must be carefully considered before use in current or next-generation gas turbines.

Before a new fuel can be used in a gas turbine it must undergo an extensive certification process, including small- and large-scale experimental validation. Key performance targets, including cold restart, altitude relight and lean blow-out behavior, determine whether a candidate fuel is suitable for use in existing and future gas turbines. However, this certification process is both time consuming and expensive. The ignition of an aeronautical burner can be decomposed in several phases (Mastorakos 2009): transition from spark to sustained kernel growth, followed by flame propagation and eventually flame stabilization. For both cold restart and altitude relight, knowledge of the ignition behavior of candidate fuels is required to ensure reliable and smooth ignition on initial startup (Lefebvre 1998) and reliable relight at altitude, where low ambient temperatures and atmospheric pressure change the ignition characteristics (Dooley 1996). Experimental results by Armstrong & Wilsted (1952) suggest the optimal location for an igniter in realistic gas turbines is along the centerline near the nozzle. However, in practical terms the injector is placed away from the nozzle, often in a suboptimal location, to improve the longevity of the igniter, and to allow for easier maintenance (Sforzo *et al.* 2014). In these circumstances, successful ignition relies on the convection and growth of an ignition kernel. The ability of computational fluid dynamics (CFD) to predict the impact of physico-chemical properties of the candidate fuels on the ignition behavior needs to be investigated to determine if CFD tools can be applied to reduce the cost and duration of the certification process. Most numerical studies of gas turbine ignition focus on the flame propagation, stabilization (Neophytou *et al.* 2012; Esclapez *et al.* 2015) and burner-to-burner propagation (Barré *et al.* 2014). A frequent assumption in these studies is that a sustained kernel is already established, thus neglecting ignition failures related to kernel formation and growth mechanisms.

In the present study, the ability of CFD tools to predict ignition kernel formation and growth at different operating conditions is investigated. Modeling the kernel formation process is challenging as it requires accounting for the transition to the plasma phase following the spark discharge to gas phase fuel oxidation chemistry (Kravchik & Sher

† Argonne National Laboratory, Argonne IL
‡ Georgia Institute of Technology, Atlanta GA

1994; Sforzo *et al.* 2015). This transition is complicated by the inherently stochastic ignition process that depends on local flow and mixture conditions and spark discharge variability. In the present study, the ignition behavior of a stratified methane mixture at different equivalent ratios (Sforzo *et al.* 2014) is investigated. This idealized flow setup contains many of the key physical characteristics which are observed in a realistic gas turbine, specifically spark ignition system with high variability and varying local flow conditions and composition. Data are available for both simple fuel (natural gas) and realistic aeronautical fuels. An important feature is that the kernel has to transit from the spark discharge location through an inert mixture prior to reaching the reactive mixture, which results in temporal separation of plasma effects and kernel combustion initiation, thereby reducing the required modeling effort.

This study represents the first step in determining if current CFD models are able to capture the ignition behavior of realistic jet fuels under cold restart and altitude relight conditions. In this prospect, a simple fuel (natural gas) is retained, that has well-established chemical behavior. The first objective of the current study is to develop a numerical model which is able to reproduce the kernel ejection phenomena observed experimentally, capturing its primary features and its stochastic variability. Based on this model, the second objective is to determine if high-fidelity simulations with finite-rate chemistry are able to correctly predict the strong dependency of the kernel ignition and growth on the operating conditions, focusing on the impact of the equivalence ratio. The third and final objective is to analyze the physical processes involved in the ignition kernel growth and behavior, and how it can be impacted by the variability of the initial conditions.

2. Experimental setup

The experimental configuration detailed in (Sforzo *et al.* 2014; Sforzo 2014) is chosen for the current study. A schematic of the facility is shown in Figure 1. It has a rectangular cross-section with a width of 54 mm and a height of 86 mm. It has been designed to investigate ignition kernel development and evolution over a minimum of 2 ms after the spark discharge, which is created by a commercial sunken igniter with a spark energy of $E_{spark} = 1.2$ J. Following the discharge, the kernel precursor is ejected into the crossflow, where it transits into a non-flammable cold air mixture (characteristic time $\tau_{transit}$) before entering into a premixed fuel-air mixture. The stratification of the crossflow into the flammable fuel-air mixture and non-flammable air mixture is imposed using two streams separated by a splitter plate, located at a height h_s from the bottom wall. A mixing layer develops downstream of the end of the splitter plate, which is located 13 mm upstream of the spark igniter.

Control over the flow velocity, equivalence ratio, crossflow inlet temperature and transient time required for the kernel to reach the flammable mixture, allows for a systematic investigation of the ignition probability over a wide range of operating conditions. Experimental measurements of the ignition probability, Schlieren imaging of the kernel, kernel trajectory and integrated OH* chemiluminescence are available for comparison with numerical data. For the present study, the fuel considered is natural gas, and is assumed to be pure methane for modeling purposes. Values for the crossflow velocity $u_{in} = 20$ m/s, crossflow temperature $T_{in} = 456$ K, and a splitter plate height $h_s = 6.4$ mm are retained and held constant throughout this study.

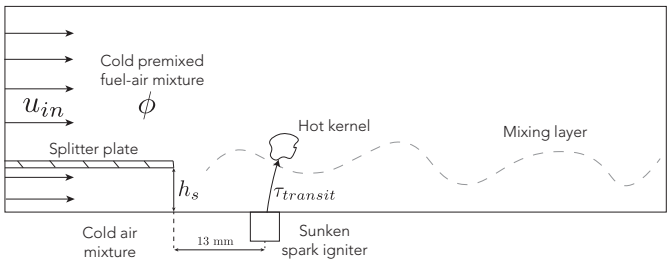

FIGURE 1. Schematic of the experimental facility. Adapted from Sforzo (2014).

3. Computational setup

3.1. *Numerics*

The simulations are performed with the finite-volume solver, CharLES^X. Temporal discretization is provided using a strong stability preserving third-order Runge-Kutta (SSP-RK3) scheme (Gottlieb *et al.* 2001) and a hybrid scheme is applied for the convective fluxes. The hybrid scheme minimizes the numerical dissipation introduced (Khalighi *et al.* 2011) and consists of a fourth-order central scheme and a second-order ENO scheme (Hickey *et al.* 2013; Ma *et al.* 2017). Chemical source terms are evaluated using finite-rate chemical kinetics with an efficient partially implicit integration method for stiff chemistry.

3.2. *Computational domain and boundary conditions*

A global view of the numerical domain is shown in Figure 2. The rectangular cross-section dimensions shown in Figure 2 are smaller than the experimental ones to reduce computational cost. It was verified that this reduction does not induce any significant confinement effects. Lateral and bottom walls are modeled with no-slip and adiabatic boundary conditions, and a constant pressure ($P = 1$ bar) condition is applied at the outlet. The domain inlet corresponds to the location where the splitter plate ends, where the air and the premixed methane-air begin mixing. To reproduce the inflow, a constant velocity of $u_{in} = 20$ m/s is applied. Turbulent velocity fluctuations are superimposed with intensity $u' = 2$ m/s (10% of the mean) based on experimental root-mean-square (rms) velocity levels (Sforzo 2014) with an integral length of $h_s/2 = 3.2$ mm. Pure air is imposed below the splitter plate height ($z < h_s$) and a premixed fuel-air mixture at the inlet temperature T_{in} is specified above. The resulting mixing field is illustrated by an instantaneous mid-plane cut of methane mass fraction in Figure 2. The kernel ejection is modeled with a temporally varying boundary condition embedded at the bottom wall, that is detailed in Section 4. The domain is discretized with a uniform grid size of $\Delta = 0.25$ mm in all directions, comprising 7 millions hexahedral elements.

3.3. *Chemical kinetics*

The chemistry is described by a reduced mechanism comprising 22 transported species and 21 species in quasi-steady state approximation. The mechanism is based on the GRI 3.0 detailed mechanism (Bowman *et al.* 1999) and describes methane-air oxidation and NO_x chemistry. This mechanism was employed in different combustion applications, such as non-premixed pilot-stabilized flames (Jaravel *et al.* 2017), stratified gas turbine burners (Jaravel *et al.* 2018) and autoignition stabilized flames (Schulz *et al.* 2017).

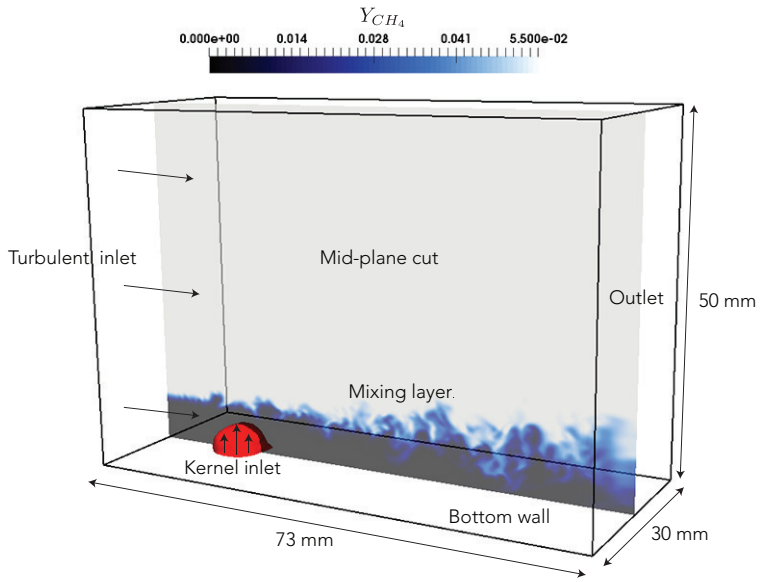

FIGURE 2. Global view of the computational domain and mid-plane cut colored by instantaneous fuel mass fraction.

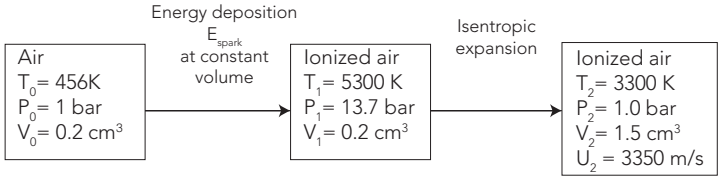

FIGURE 3. Sucessive thermodynamics state for the idealized zero-dimensional model.

4. Kernel ejection modeling

The actual kernel formation process comprises an energy deposition phase with plasma formation in the igniter cavity followed by a rapid expansion into the main flow. Correctly describing this process requires an accurate description of the plasma physics and highly compressible phenomena (Sforzo *et al.* 2015) that are beyond the scope of this work. Therefore, only the post-expansion behavior of the kernel is considered in the three-dimensional simulation. The properties of the post-expansion state of the kernel are obtained from the zero-dimensional model from Sforzo *et al.* (2014) described below. The kernel is assumed to be at equilibrium. This hypothesis appears to be reasonable when comparing the typical lifetime of plasma atomic species $[O(1-10\,\mu\text{s})]$ to the transit time of the kernel to the flammable region $[\tau_{transit} = O(100\,\mu\text{s})]$ (Mastorakos 2017).

4.1. *Zero-dimensional thermodynamic model*

The model describes the kernel formation by successive idealized transformations, that are summarized in Figure 3. In a first step, the air inside the sunken igniter ($V = 0.2$ cm^3) receives an energy deposition, $E_{spark} = 1.2$ J, from the spark discharge. Assuming an isochoric heat addition, the intermediate equilibrium state of the kernel is computed using the air plasma mechanism from Schulz *et al.* (2012), leading to high post-discharge

	X_{N_2}	X_{O_2}	X_{NO}	X_N	X_O	X_{NO_2}	X_{N_2O}
Air plasma	0.72	0.12	0.049	7.7×10^{-5}	0.11	[-]	[-]
Reduced	0.74	0.14	0.054	[-]	0.062	3×10^{-5}	4.4×10^{-6}

	$X_{N_2^+}$	$X_{O_2^+}$	X_{NO^+}	X_{N^+}	X_{O^+}	X_{e^-}
Air plasma	0	0	1.9×10^{-7}	0	0	1.9×10^{-7}
Reduced	[-]	[-]	[-]	[-]	[-]	[-]

TABLE 1. Post expansion ($T = 3300$ K, $P = 1$ bar) kernel equilibrium kernel composition in mole fractions. Comparison between air plasma chemistry and reduced methane-air chemistry.

temperature ($T = 5300$ K) and pressure ($P = 13$ bar). The second step of the process is an isentropic expansion of the ionized mixture to the main flow pressure ($P = 1$ bar) leading, under the assumption of chemical equilibrium, to a final temperature of $T = 3300$ K that is used as the initial condition for the simulations. The resulting composition given in Table 1 shows that the contribution of ionized species is not significant at this temperature and the comparison with equilibrium obtained from the reduced mechanism is in very good agreement in terms of the initial composition. Thus, in the present study the reduced mechanism without considering plasma ionized species is utilized. From mass and total enthalpy conservation, the final volume (1.5 cm^3) and velocity of the kernel (3350 m/s) can also be deduced. However, only a fraction of the total kernel volume may actually enter into the main chamber, and various losses (shock wave, etc.) can reduce the initial kernel velocity. Therefore, these two values can be used as initial conditions, which are later adjusted by matching the estimation of kernel volume and trajectory obtained from high-speed Schlieren imaging data.

4.2. *Pulsed kernel inlet definition*

To model the ejection of the post-expansion kernel, a pulsed inlet boundary condition is used at the bottom wall. The kernel composition is taken from the equilibrium composition at $T = 3300$ K for the reduced mechanism given in Table 1. The controlling parameters for the kernel injection are a characteristic velocity U_{kernel}, the injection surface $S = \pi D^2/4$ and the characteristic time of the pulse τ_{pulse}. The kernel injection diameter is taken to be equal to the diameter of the sunken igniter box, $D = 5$ mm. This value is also consistent with the equivalent diameter of the kernel estimated from Schlieren visualization, as shown later in Section 4.3. To reproduce the spherical shape of the kernel, a spherical profile is imposed on the boundary normal velocity

$$u_n = \mathcal{M}(t)\, U_{kernel} \sqrt{1 - (2r/D)^2}\,, \tag{4.1}$$

where r is the radial distance from the injection surface center, and $\mathcal{M}(t)$ is a function of time. To mimic the kernel ejection, a velocity jump is imposed at time $t = 0$, which is maintained for a duration $t = \tau_{pulse}$ and then the velocity decreases linearly towards zero from τ_{pulse} to $2\tau_{pulse}$.

4.2.1. *Kernel inlet forcing*

In the experiments, the kernel trajectory is almost independent of the crossflow, but nonetheless a significant variability of transit time is observed, which may be attributed to stochastic variability from one spark discharge to another. For the conditions considered

here ($h_s = 6.4$ mm), the mean transit time to the splitter plate height is 40 μs (Sforzo 2014), and a dispersion of ± 10 μs is reported, which corresponds to a typical deviation of 25%. To mimic this dispersion numerically, a random forcing of 20% intensity with a length scale corresponding to the kernel size is imposed on the velocity at the kernel boundary condition.

4.3. *Cold flow kernel ejection: parameters calibration*

The aim of the calibration is to find suitable values for the remaining controlling parameters of the kernel boundary conditions (U_{kernel} and τ_{pulse}), based on comparisons with experimental results. To do so, several non-reactive simulations are performed for one reference case ($\phi = 1.0$), as the initial kernel volume and trajectory are independent of the operating conditions considered. From these, the boundary conditions are selected by matching two metrics extracted from Schlieren imaging at early instants ($t = 50 - 300$ μs): (i) kernel volume, and (ii) kernel trajectory. The kernel trajectory is extracted from the high-speed Schlieren imaging by edge tracking. Similarly, the kernel volume is evaluated by computing the equivalent diameter of the kernel surface resulting from edge detection. An analogue methodology is used in the simulations, where the kernel boundary is defined by thresholding Line Of Sight (LOS) integration of either a passive scalar tracing the kernel ejection or numerical Schlieren ($\nabla\rho/\rho$).

The kernel volume V_{ker} issuing from the boundary condition scales as $V_{ker} \propto U_{kernel}\Delta t$, whereas the kernel trajectory scales with the injected momentum $J \propto U_{kernel}^2 \Delta t$. Thus, from a first simulation with the parameters provided by the zero-dimensional model, the two parameters can be adjusted based on this scaling to match the two criteria. Final values $U_{kernel} = 2000$ m/s and $\tau_{pulse} = 75$ μs are retained. The comparison of one experimental kernel injection and an unforced (no kernel velocity fluctuations) numerical sequence is shown in Figure 4. Note that bright emission obscures Schlieren results at early instants ($t = 20, 40$ μs). The comparison shows that a good qualitative agreement is obtained in terms of kernel size, shape and temporal evolution, with similar transit time to the splitter height. The comparison of LOS integration of passive scalar and numerical Schlieren shows that they yield similar definitions of the kernel boundaries. The sensitivity of boundary definition is also illustrated by showing the kernel edge obtained for two different threshold values (5×10^{-4} and 2×10^{-3}) for the LOS integration of passive scalar [Figure 4 (ii)].

A quantitative comparison of kernel diameter is performed by comparing Schlieren estimation and LOS integration for the unforced kernel injection, and five forced cases with 20% random velocity fluctuations at the kernel inlet. The LOS integration of the passive scalar and numerical Schlieren yield similar diameter size estimation; however, the former is preferred as it is less sensitive to the threshold selected due to lower numerical noise. The comparison of experimental and numerical data in Figure 5 shows a significant sensitivity of the diameter estimation to the threshold value. It is close to the experimental range regardless of the threshold and the agreement is largely acceptable, given the overall uncertainty on the diameter estimation. Also, the forcing has a marginal impact on the resulting volume; the diameters obtained for the five forced cases do not significantly differ from the unforced cases. Similarly, the comparison of trajectories is shown in Figure 6 for the kernel centroid distance for the bottom wall and Figure 7 for the leading edge. The trajectories are insensitive to the threshold value, and the overall agreement of centroid and leading edge trajectory is satisfactory. As shown by the trajectory of the five forced cases, the forcing leads to a dispersion of the trajectories around the unforced case. The dispersion level can be quantified by evaluating the transit time

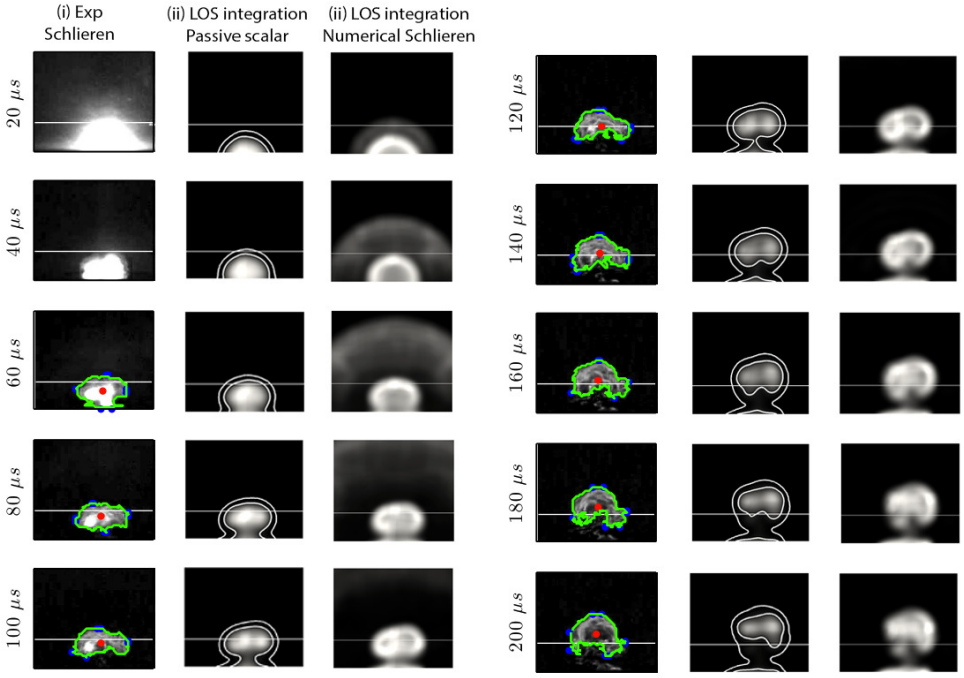

FIGURE 4. Time progression sequence of a kernel trajectory. Comparison between (i) experimental Schlieren imaging with edge tracking lines, (ii) LOS integration of passive scalar with kernel edge defined by two different threshold values (5×10^{-4} and 2×10^{-3}) and (iii) LOS integration of numerical Schlieren for an unforced kernel injection. The horizontal white line indicates the height of the splitter plate.

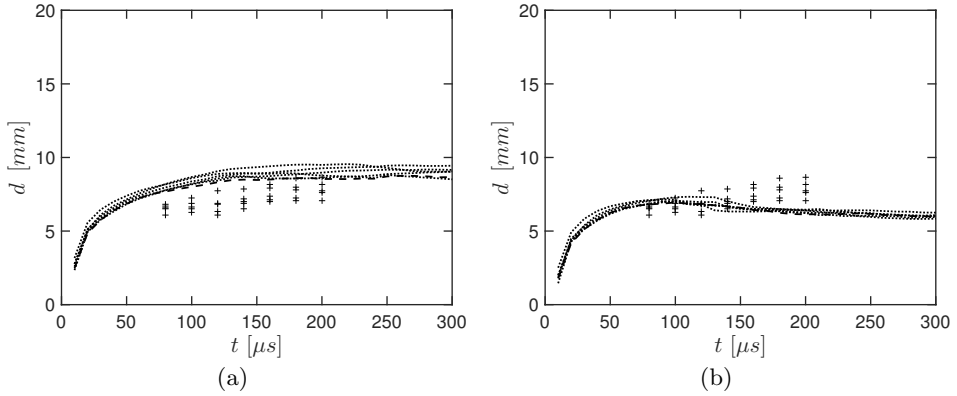

FIGURE 5. Kernel diameter vs. time. Comparison between Schlieren images (symbols), unforced case (−−) and five forced cases (· · ·) for two different threshold values, namely (a) $= 5 \times 10^{-4}$ and (b) $= 2 \times 10^{-3}$.

of the kernel leading edge and centroid to the splitter height. The comparison with experiments in Figure 8 shows good agreement for both leading edge and centroid transit time for the unforced cases, which falls within the experimental range. The dispersion obtained for the five forced cases is also consistent with the experimental levels.

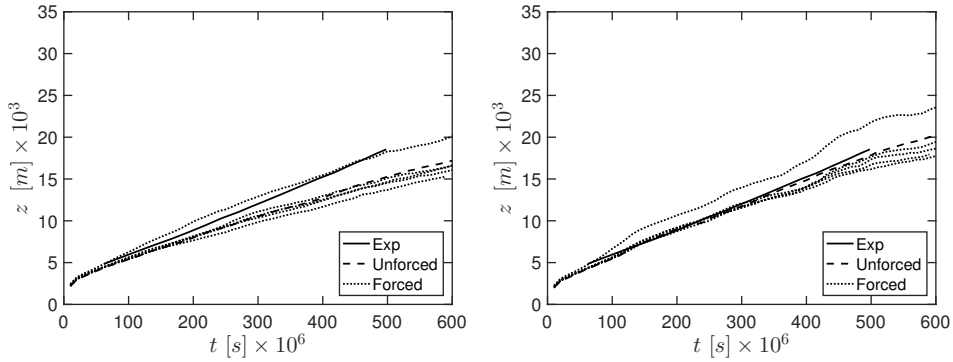

FIGURE 6. Kernel centroid distance from wall vs. time for two different threshold values. Comparison between fit from experiments (—), unforced case (−−) and five forced cases $(\cdots)$ for two different threshold values, namely (a) $= 5 \times 10^{-4}$ and (b) $= 2 \times 10^{-3}$.

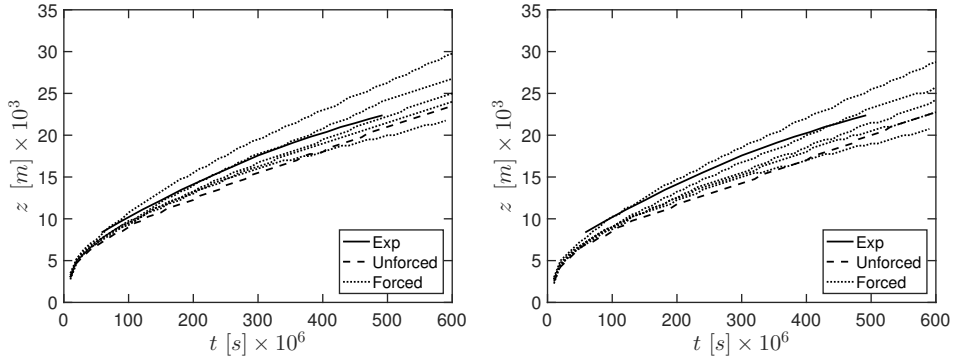

FIGURE 7. Leading edge of the kernel distance from wall vs. time for two different threshold values. Comparison between fit from experiments (—), unforced case (−−) and five forced cases $(\cdots)$ for two different threshold values, namely (a) $= 5 \times 10^{-4}$ and (b) $= 2 \times 10^{-3}$.

5. Reactive cases

For reacting simulations, three operating conditions are selected to cover the range of equivalence ratios that were studied experimentally. The evolution of ignition probability for different equivalence ratios is shown in Figure 9. It peaks for slightly rich conditions around $\phi = 1.2$. For the numerical study, three operating conditions are selected: $\phi = 0.6$, which corresponds to zero ignition probability in the experiments; $\phi = 1.2$, which corresponds to maximum probability of ignition ($P_{ign} = 80\%$) and $\phi = 1.0$, which has an intermediate behavior with 50% ignition probability. These cases are chosen to produce dramatically different ignition behaviors.

For each equivalence ratio, three kernel ejection realizations are simulated. Note that the initial condition is a randomly selected initial cold flow solution, different for each simulation, to capture the stochastic impact of the mixing layer fluctuations.

5.1. *Ignition behavior*

A first metric to assess the kernel transition to a propagating flame is the temporal evolution of total heat release rate in the domain. Figure 10 shows the comparison for

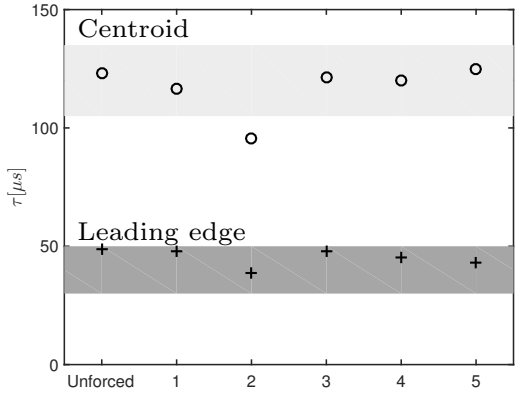

FIGURE 8. Transit time of kernel leading edge (+) and kernel centroid (∘) to the splitter height for the unforced case and five forced cases. The shaded areas indicate the experimental range.

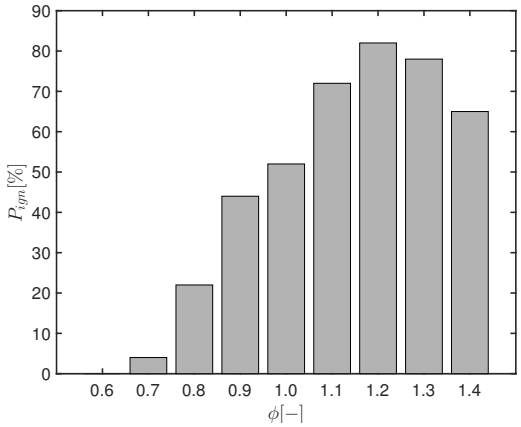

FIGURE 9. Experimental ignition probability vs. equivalence ratio. Adapted from Sforzo (2014).

the different operating conditions. For all cases, a steep increase is observed at early instants ($t \simeq 0-150$ μs), corresponding to the kernel transit phase from the bottom wall to the mixing layer. In this phase, the heat release rate is mainly due to the exothermic recombination of radicals initially present in the kernel. A second phase is observed for $t \simeq 100-500$ μs. In this time interval, the kernel travels through the premixed mixture, and thus starts entraining reactive mixture and mixes it with the hot inert gases. Around $t = 500$ μs, the temperature fields of Figure 11 show that the kernel is well inside the premixed mixture but has not grown significantly. Some ignition events occur, as shown by the heat release rate field in Figure 12. They preferentially occur in the downstream (right part) of the kernel. This region of the kernel is not directly exposed to the incoming crossflow. It results in lower strain rates and entrainment rate, leading to conditions that may be more favorable to ignition. From these local ignition events, the full kernel ignition may eventually occur, which translates into a steep increase of heat release rate for $\phi = 1.0$ and 1.2 after 500 μs (Figure 10), and significant spatial growth of the hot kernel region (Figure 11) and reacting zone (Figure 11) for $t > 500$ μs, indicating successful ignition events for these operating conditions. Conversely for $\phi = 0.6$, a plateau of heat release is observed, and the kernel hot region shrinks under

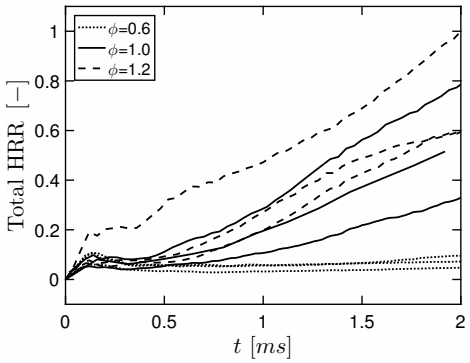

FIGURE 10. Total heat release rate (normalized by the overall maximum value) vs. time for the ensemble of cases.

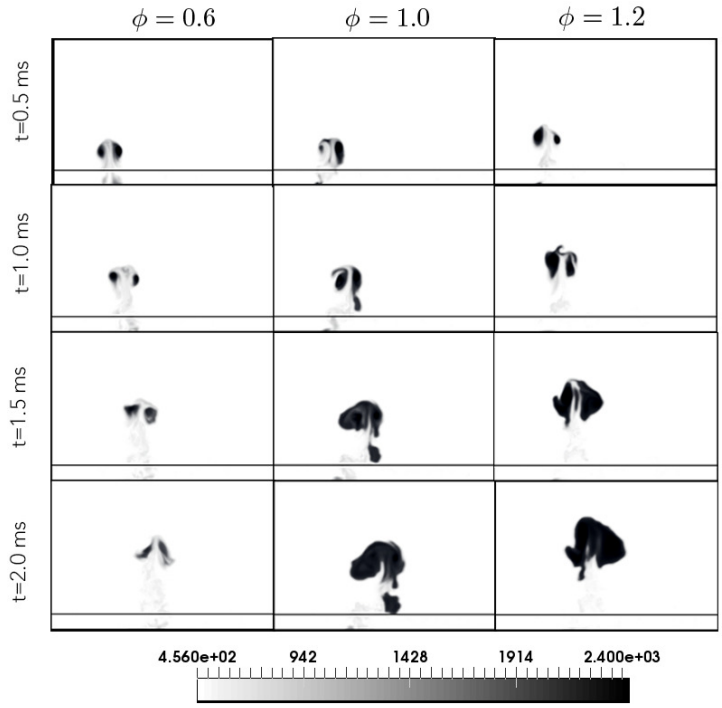

FIGURE 11. Temperature field (K) in the mid-plane at four different instants for three operating conditions ($\phi = \{0.6, 1.0, 1.2\}$). The horizontal line indicates the height of the splitter plate.

the effect of mixing with the reactive mixture, without any onset of a strongly reacting layer characteristic of a self-propagating kernel.

5.2. *Detailed analysis of ignition sequence*

A detailed analysis of the ignition sequence is performed for two ignition realizations at $\phi = 0.6$ and $\phi = 1.0$ previously shown in Figure 11 and Figure 12. Three tracers are used to track mixture from the kernel inlet (ξ_{kernel}), the inert part (ξ_{inert}) and premixed fuel-air mixture part (ξ_f) of the crossflow, defined equal to 1 at their respective inlet

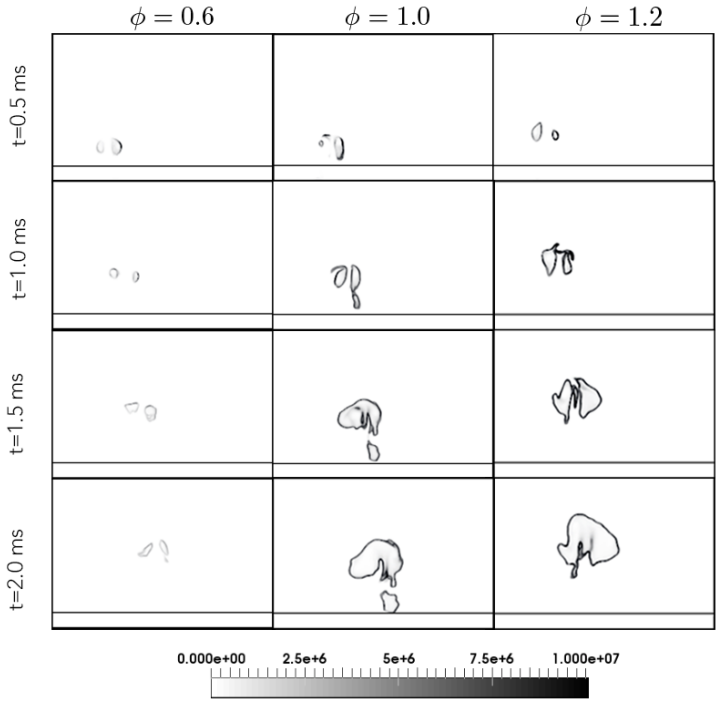

FIGURE 12. Heat release rate field (K/m^3/s) in the mid-plane at several instants for three realizations at three different operating conditions ($\phi = \{0.6, 1.0, 1.2\}$). The horizontal line indicates the height of the splitter plate.

boundary condition. The mixture fraction is evaluated from the fuel stream tracer as

$$Z = Y^f_{CH4}\xi_f \,, \tag{5.1}$$

where Y^f_{CH4} corresponds to premixed fuel-air crossflow mass fraction. Mean kernel tracer, mean temperature and integrated heat release rate are extracted in the kernel region from instantaneous solutions at different instants ($t = 0.5, 1, 1.5, 2$ ms) and conditioned on mixture fraction Z. The conditional mean of the kernel injection tracer is shown in Figure 13. The gap between kernel tracer and the binary mixing line (kernel/crossflow fuel-air stream) indicates the level of dilution of the kernel by the inert cold air. Similar mixing behavior is obtained for the lean and stoichiometric cases. The dilution of the kernel by cold air stabilizes after the kernel has fully entered in the fuel-air crossflow ($t > 1$ ms), representing more than 50% of the total kernel composition. The evolution of conditional temperature is shown in Figure 14. For the lean case [Figure 14(a)], at $t = 0.5$ ms the temperature is initially high at low mixture fraction, and decreases quasi-linearly with mixture fraction, because of mixing of hot air from the kernel with the fuel-air mixture. This creates favorable conditions for ignition at low mixture fraction, with a peak in conditional integrated heat release rate around $Z = 0.008$, as shown in Figure 15. At subsequent instants, because of fuel-air mixture entrainment, the mixture fraction distribution is shifted towards richer mixtures. Accordingly, the conditional integrated heat release rate [Figure 15(a)] shifts towards richer regions, but the total integrated heat release plateaus as shown previously in Figure 10. As a result, the temperature remains close to the mixing levels [Figure 14(a)] with no significant increase in the reaction

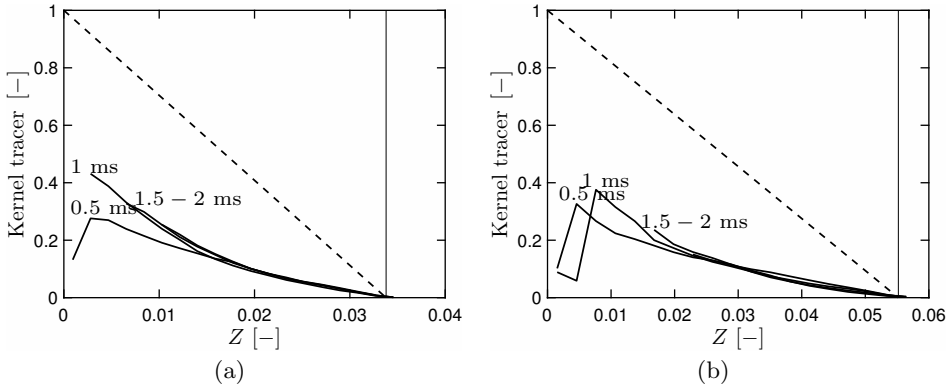

FIGURE 13. Mean kernel tracer conditioned on mixture fraction at four different instants ($t = 0.5, 1, 1.5, 2$ ms) for (a) lean conditions ($\phi = 0.6$) and (b) stoichiometric conditions ($\phi = 1.0$). The vertical line indicates the mixture fraction of the crossflow fuel-air stream. The dashed line indicates the binary mixing line between kernel and fuel stream.

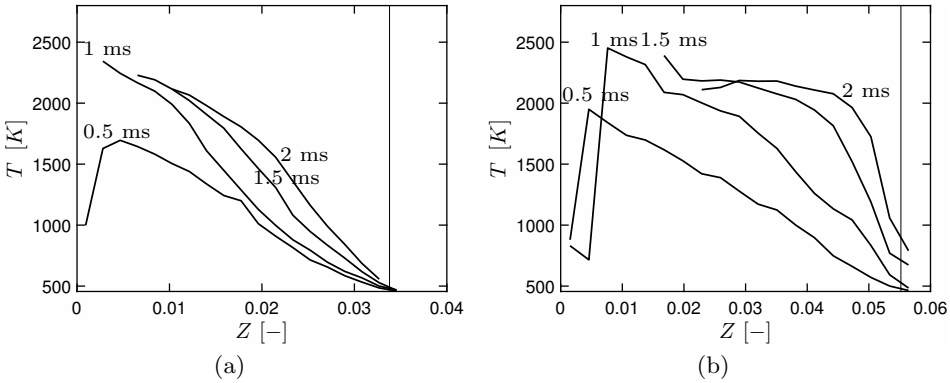

FIGURE 14. Mean temperature conditioned on mixture fraction at four different instants ($t = 0.5, 1, 1.5, 2$ ms) for (a) lean conditions ($\phi = 0.6$) and (b) stoichiometric conditions ($\phi = 1.0$). The vertical line indicates the mixture fraction of the crossflow fuel-air stream.

region, indicating that no transition to a sustained flame propagation occurs. For the stoichiometric case, a similar behavior is observed for mean temperature [Figure 14(b)] and integrated heat release rate [Figure 15(b)] for the first instant ($t = 0.5$ ms). However, in this case, the integrated heat release rate dramatically increases as it travels towards higher mixture fractions. At $t = 2$ ms, the heat release rate peaks near the mixture fraction of the fuel stream, indicating that the kernel has almost transitioned to a premixed burning mode at the crossflow fuel-air stream equivalence ratio. This is supported by the mean temperature evolution [Figure 14(b)], evolving from mixing levels at $t = 0.5$ ms to reach levels close stoichiometric adiabatic flame temperature at $t = 2$ ms. Further investigations are needed to understand how the dilution by cold air can impact this transition from local ignition to sustained flame propagation, and if it can result in failed transition for cases with high kernel dilution.

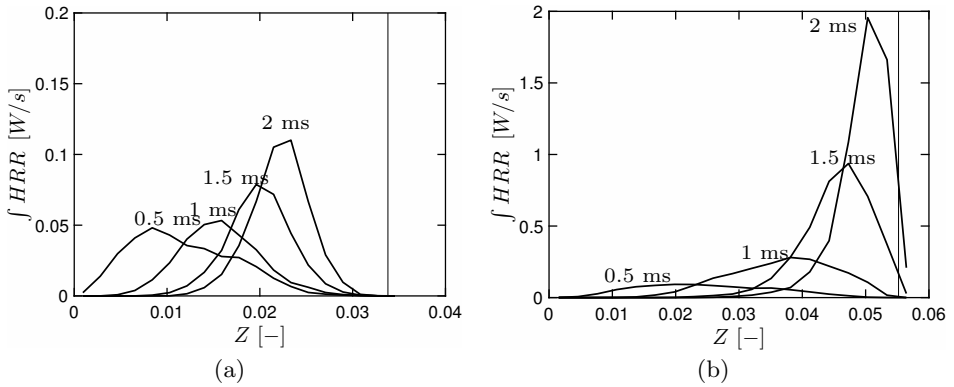

FIGURE 15. Integrated heat release rate conditioned on mixture fraction at four different instants ($t = 0.5, 1, 1.5, 2$ ms) for (a) lean conditions ($\phi = 0.6$) and (b) stoichiometric conditions ($\phi = 1.0$). The vertical line indicates the mixture fraction of the crossflow fuel-air stream.

6. Conclusion and perspectives

In this work, computations of multiple realizations of kernel ejection inside a crossflow are performed for different operating conditions. Kernel injection parameters are defined based on a zero-dimensional thermodynamic model and a calibration step based on comparison between temporal evolution of inert kernel and experimental results. Then, nine kernel ejection realizations are simulated at three different operating conditions with varying cross-flow equivalence ratio. The strong dependency of the ignition behavior to the crossflow equivalence ratio is well reproduced numerically, with systematic ignition failures for the leanest conditions. Significant variability is also observed from one realization to another. From a detailed analysis of the kernel structure, it appears that the ignition is initially triggered in lean conditions for all cases where the mixture temperature is high because of the fuel-air mixing with hot kernel gases. Depending on the conditions, it may propagate towards richer mixtures close to the equivalence ratio of the premixed fuel-air stream, eventually leading to a sustained premixed propagation mode.

Further analysis is needed to fully understand the variability from one case to another for a given set of operating conditions. In particular, high kernel transit time can result in more entrainment of cold air, hampering the ignition process and transition to premixed flame propagation. Correlations between transit time, dilution and ignition behavior will be established in future work. By significantly extending the amount of realizations simulated for each operating point, probabilistic behavior could also be assessed numerically. In addition, this study could be extended from natural gas to more realistic aeronautical fuels (Sforzo *et al.* 2016) to understand the impact of fuel variability on ignition kernel formation and growth.

REFERENCES

ARMSTRONG, J. C. & WILSTED, H. D. 1952 *Investigation of several techniques for improving altitude starting limits of turbojet engines.* NACA Res. Memo. E52I03.

BARRÉ, D., ESCLAPEZ, L., CORDIER, M., RIBER, E., CUENOT, B., STAFFELBACH, G., RENOU, B., VANDEL, A., GICQUEL, L. Y. M. & CABOT, G. 2014 Flame propagation in aeronautical swirled multi-burners: Experimental and numerical investigation. *Combust. Flame* **161**, 2387–2405.

Bowman, C., Frenklach, M., Gardiner, W. & Smith, G. 1999 The GRI 3.0 chemical kinetic mechanism. *http://www.me.berkeley.edu/gri_mech/*.

Dooley, K. A. 1996 Continuous plasma ignition system. US Patent 5,587,630.

Esclapez, L., Riber, E. & Cuenot, B. 2015 Ignition probability of a partially premixed burner using LES. *Proc. Combust. Inst.* **35**, 3133–3141.

Gottlieb, S., Shu, C.-W. & Tadmor, E. 2001 Strong stability-preserving high-order time discretization methods. *SIAM Rev.* **43**, 89–112.

Hickey, J.-P., Ma, P. C., Ihme, M. & Thakur, S. 2013 Large eddy simulation of shear coaxial rocket injector: Real fluid effects. *AIAA Paper* #2013-4071.

Jaravel, T., Riber, E., Cuenot, B. & Bulat, G. 2017 Large Eddy Simulation of an industrial gas turbine combustor using reduced chemistry with accurate pollutant prediction. *Proc. Combust. Inst.* **36**, 3817–3825.

Jaravel, T., Riber, E., Cuenot, B. & Pepiot-Desjardins, P. 2018 Prediction of flame structure and pollutant formation of Sandia flame D using Large Eddy Simulation with direct integration of chemical kinetics. *Combust. Flame* **188**, 180–198.

Khalighi, Y., Nichols, J. W., Lele, S., Ham, F. & Moin, P. 2011 Unstructured large eddy simulation for prediction of noise issued from turbulent jets in various configurations. In *17th AIAA/CEAS Aeroacoustics Conference*. Portland, OR.

Kravchik, T. & Sher, E. 1994 Numerical modeling of spark ignition and flame initiation in a quiescent methane-air mixture. *Combust. Flame* **99**, 635–643.

Lefebvre, A. H. 1998 *Gas Turbine Combustion*. CRC Press.

Ma, P. C., Lv, Y. & Ihme, M. 2017 An entropy-stable hybrid scheme for simulations of transcritical real-fluid flows. *J. Comput. Phys.* **340**, 330–357.

Mastorakos, E. 2009 Ignition of turbulent non-premixed flames. *Prog. Energy Combust. Sci.* **35**, 57–97.

Mastorakos, E. 2017 Forced ignition of turbulent spray flames. *Proc. Combust. Inst.* **36**, 2367–2383.

Neophytou, A., Richardson, E. S. & Mastorakos, E. 2012 Spark ignition of turbulent recirculating non-premixed gas and spray flames: A model for predicting ignition probability. *Combust. Flame* **159**, 1503–1522.

Schulz, J. C., Gottiparthi, K. C. & Menon, S. 2012 Ionization in gaseous detonation waves. *Shock Waves* **22**, 579–590.

Schulz, O., Jaravel, T., Poinsot, T., Cuenot, B. & Noiray, N. 2017 A criterion to distinguish autoignition and propagation applied to a lifted methane-air jet flame. *Proc. Combust. Inst.* **36**, 1637–1644.

Sforzo, B., Dao, H., Wei, S. & Seitzman, J. 2016 Liquid fuel composition effects on forced, non-premixed ignition. *J. Eng. Gas Turb. Power* **139**, 1–8.

Sforzo, B., Kim, J., Jagoda, J. & Seitzman, J. 2014 Ignition probability in a stratified turbulent flow with a sunken fire igniter. *J. Eng. Gas Turb. Power* **137**, 011502.

Sforzo, B., Lambert, A., Kim, J., Jagoda, J., Menon, S. & Seitzman, J. 2015 Post discharge evolution of a spark igniter kernel. *Combust. Flame* **162**, 181–190.

Sforzo, B. A. 2014 *High energy spark ignition in non-premixed flowing combustors*. Ph.D. Thesis, Georgia Institute of Technology.